300-GHz InP HBT Oscillators Based on Common-Base Cross-Coupled Topology

Jongwon Yun, Daekeun Yoon, Hyunchul Kim, and Jae-Sung Rieh, *Senior Member, IEEE*

***Abstract*—Two fundamental-mode oscillators operating around 300 GHz, a fixed-frequency oscillator and a voltage-controlled oscillator (VCO), have been developed in this work based on a 250-nm InP heterojunction bipolar transistor (HBT) technology. Both oscillators adopted the common-base configuration for the cross-coupled oscillator core, providing higher oscillation frequency compared to the conventional common-emitter cross-coupled topology. The fabricated fixed-frequency oscillator and the VCO exhibited oscillation frequency of 305.8 GHz and 298.1–316.1 GHz (18-GHz tuning range) at dc power dissipation of 87.4 and 88.1 mW, respectively. The phase noise of the fixed-frequency oscillator was measured to be -116.5 dBc/Hz at 10 MHz offset. The peak output power of 5.3 dBm (3.8% dc-to-RF efficiency) and 4.7 dBm (3.2% dc-to-RF efficiency) were respectively achieved for the two oscillators, which are the highest reported power for a transistor-based single oscillator beyond 200 GHz.**

***Index Terms*—Frequency control, heterojunction bipolar transistors (HBT), voltage-controlled oscillators (VCO).**

I. Introduction

THE terahertz band presents promising applications in various scientific fields such as imaging, spectroscopy, biochemical detection, radio astronomy, broadband communication, and military applications [1], [2]. These growing interests toward the THz band boost motivations for the implementation of THz systems, particularly based on the semiconductor devices owing to their advantages such as small volume, low cost, low power dissipation, and so forth. One major component of THz systems is the signal source, which can be used for transmitters as well as local oscillators in the heterodyne architecture. For this reason, the development of high-performance semiconductor oscillators has been a major challenge, and lots of efforts have been made to improve their operation frequency, output power, as well as the phase noise. Frequency tunability is also a desired feature for many applications, leading to extensive studies on voltage-controlled oscillator (VCO) development.

While there have been various types of THz oscillators successfully implemented based on semiconductor diodes [3]–[5], transistor-based oscillators have remained for relatively lower frequency regime due to their limit in device speed. However, transistor-based oscillators are attractive from many viewpoints including the fact that they can be implemented with conventional semiconductor process technologies and thus can be compatible with other electronic parts. This is the principal advantage of transistor oscillators over other approaches for THz signal sources. Recently, there have been significant improvements in transistor operation speed in terms of f_T (cutoff frequency) and $f_{\max}$ (maximum oscillation frequency) with both Si and III-V technologies. While the improvements have been remarkable for Si-based technologies [6], [7], III-V technologies traditionally have showed higher device speed, and the $f_{\max}$ of III-V transistors of today now exceeds 1 THz [8], [9].

The device speed improvements in III-V technologies have led to the development of several fundamental-mode III-V oscillators operating beyond 300 GHz. Based on the InP HBT technology, a fundamental-mode oscillator operating up to 573.1 GHz with an output power of -19.2 dBm [10] and a 325-GHz VCO with an output power of -5 dBm [11] have been reported. With the InP HEMT technology, a 330-GHz oscillator with an output power of -5.7 dBm was reported in [12]. It is noted that oscillators operating beyond 300 GHz based on Si-based technologies have also been reported [13]–[17], but most of them are based on harmonic mode operation, resulting in rather low output power. Some groups have reported power combining from multiple oscillators leading to a high output power, but they tend to consume large dc power and need additional combining networks [18]–[20]. There have also been reports on multiplier-based signal sources working beyond 300 GHz [21]–[25], but most of them need an external low-frequency signal source for operation and suffer from increased chip size and dc power dissipation.

This paper introduces two high-power fundamental-mode oscillators based on a 250-nm InP HBT technology operating around 300 GHz, which adopt the common-base configuration for the oscillator core instead of the common-emitter configuration typically used. The paper is structured in the following way. In Section II, a comparison is made based on both analytic and simulation approaches between common-base (CB) and common-emitter (CE) configurations for the oscillator core. Description of the proposed circuits, one fixed-frequency oscillator and the other VCO, is also provided. In Section III, measurement results of the fabricated oscillators are presented, followed by Section IV, in which the application of the fabricated oscillator to THz imaging is presented. Finally, the conclusion of this paper is given in Section V.

Manuscript received May 22, 2014; revised September 09, 2014; accepted October 12, 2014. Date of publication November 06, 2014; date of current version December 02, 2014. This work was supported by the National Research Foundation under a grant funded by the Korea government (MEST) (2012R1A2A1A01005584) and Samsung Electronics.

J. Yun, D. Yoon, and J.-S. Rieh are with the School of Electrical Engineering, Korea University, Seoul 136-713, Korea (e-mail: jsrieh@korea.ac.kr).

H. Kim is with the Virginia Polytech Institute and State University, Blacksburg, VA 24061 USA.

Color versions of one or more of the figures in this paper are available online at http://ieeexplore.ieee.org.

Digital Object Identifier 10.1109/TMTT.2014.2364608

0018-9480 © 2014 IEEE. Personal use is permitted, but republication/redistribution requires IEEE permission.
See http://www.ieee.org/publications_standards/publications/rights/index.html for more information.

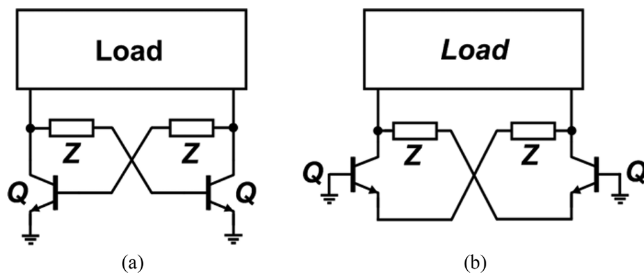

Fig. 1. Conceptual schematics of cross-coupled oscillators. (a) Conventional topology based on CE configuration. (b) Proposed topology based on CB configuration.

II. Circuit Design

One of the most popular types for the transistor-based oscillators is the LC cross-coupled oscillator. As shown in Fig. 1(a), its oscillator core is typically based on the cross-coupling of two differential transistors with CE configuration, where the collector is connected to the base of the other transistor, optionally through a phase delay component Z. On the other hand, considering the fact that the CB configuration is widely applied for amplifiers, especially for high-frequency applications, one can envision that an oscillator core can employ the cross-coupling of two transistors based on CB configuration, which is the main proposal in this paper. Fig. 1(b) shows the proposed topology, where the collector is connected to the emitter of the other transistor through an optional phase delay component. In this section, we present a qualitative comparison between the two types of oscillator topologies, followed by quantitative analyses for the oscillation frequency and startup condition. The results from the analyses are compared with simulation results, and then the detailed circuit schematic of the oscillator designed in this work is provided.

A. CB Versus CE for Cross-Coupling: Qualitative Comparison

The basic operation of a cross-coupled oscillator core can be explained with the help of Fig. 2, which simplifies the core as a series connection of two amplifiers. Each amplifier is composed of a transistor (Q_1 or Q_2) and an interstage phase delay component $\Delta\phi$, which comprises passive inductive and capacitive elements. With this description of an oscillator, the Barkhausen criteria for oscillation become $|H(j\omega)|^2 \geq 1$ and $\angle H(j\omega) = n\pi (n = 1, 3, 5, \ldots)$ where $H(j\omega)$ is the transfer function of a single amplifier stage as shown in Fig. 2. Note that n needs to be an odd integer for cross-coupled cores to meet the condition for the differential operation of Q_1 and Q_2.

With the phase characteristics of CB and CE amplifiers, we can roughly estimate the oscillation frequency of the cross-coupled oscillators based on both configurations. Fig. 3 shows the typical profiles of the phase difference across a transistor over the frequency when operated with CB and CE configurations. It is noted that the curves were obtained with the simulation of an actual transistor used in this study for the oscillator design. For transistors in CE configuration, the phase difference starts at 180° from dc condition and gradually decreases with increasing frequency. On the other hand, transistors in the CB configuration exhibit an initial phase difference of 0° at dc and decreases with increasing frequency. To meet the Barkhausen criteria for the phase given above, each amplifier, which is composed of

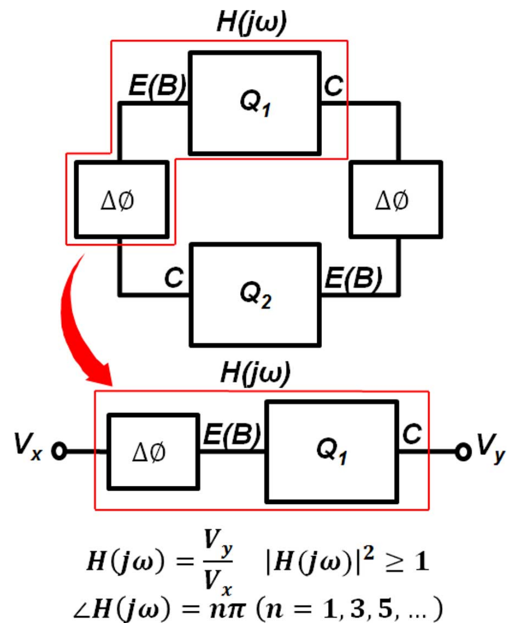

Fig. 2. Simplified diagram of a cross-coupled oscillator core and the oscillation condition.

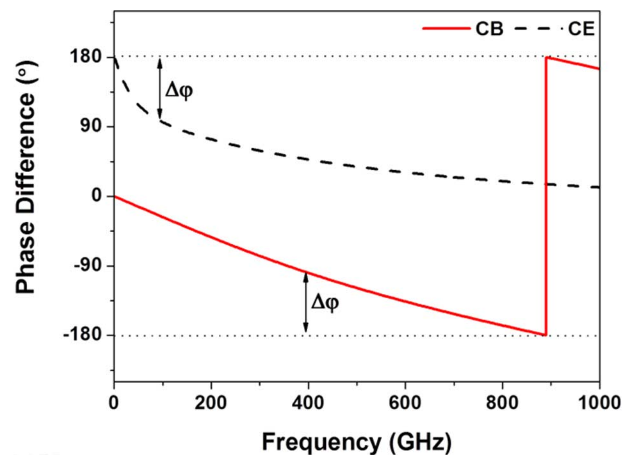

Fig. 3. Trend of the phase difference between the input and output of a CB and CE amplifier, where $\Delta\phi$ indicates additional phase shift caused by feedback and load components. The curves are obtained from simulation of the device actually employed for the oscillator developed in this paper.

a transistor and a phase delay component, should show a total phase difference of 180° (or its odd integer multiples). Hence, the oscillation will occur when the sum of the delay by the transistor alone and the delay by the delay component ($\Delta\phi$) becomes 180° (or its odd integer multiples). With moderate values of $\Delta\phi$, one can expect that such a condition will be met at a frequency point rather in the vicinity of the frequency where the delay by the transistor alone is 180°. With this conjecture, we can expect the oscillation frequency for the CE configuration would be lower than that of the CB configuration because such frequencies for the 180° shift across a transistor falls on dc and $\sim$ 900 GHz for the transistor in CE and CB configurations, respectively, as can be seen from Fig. 3. It is noted that the Barkhausen criteria dictates that the gain across an amplifier needs to be higher than unity in addition to the phase requirement. In this sense, it can be argued that the CB configuration

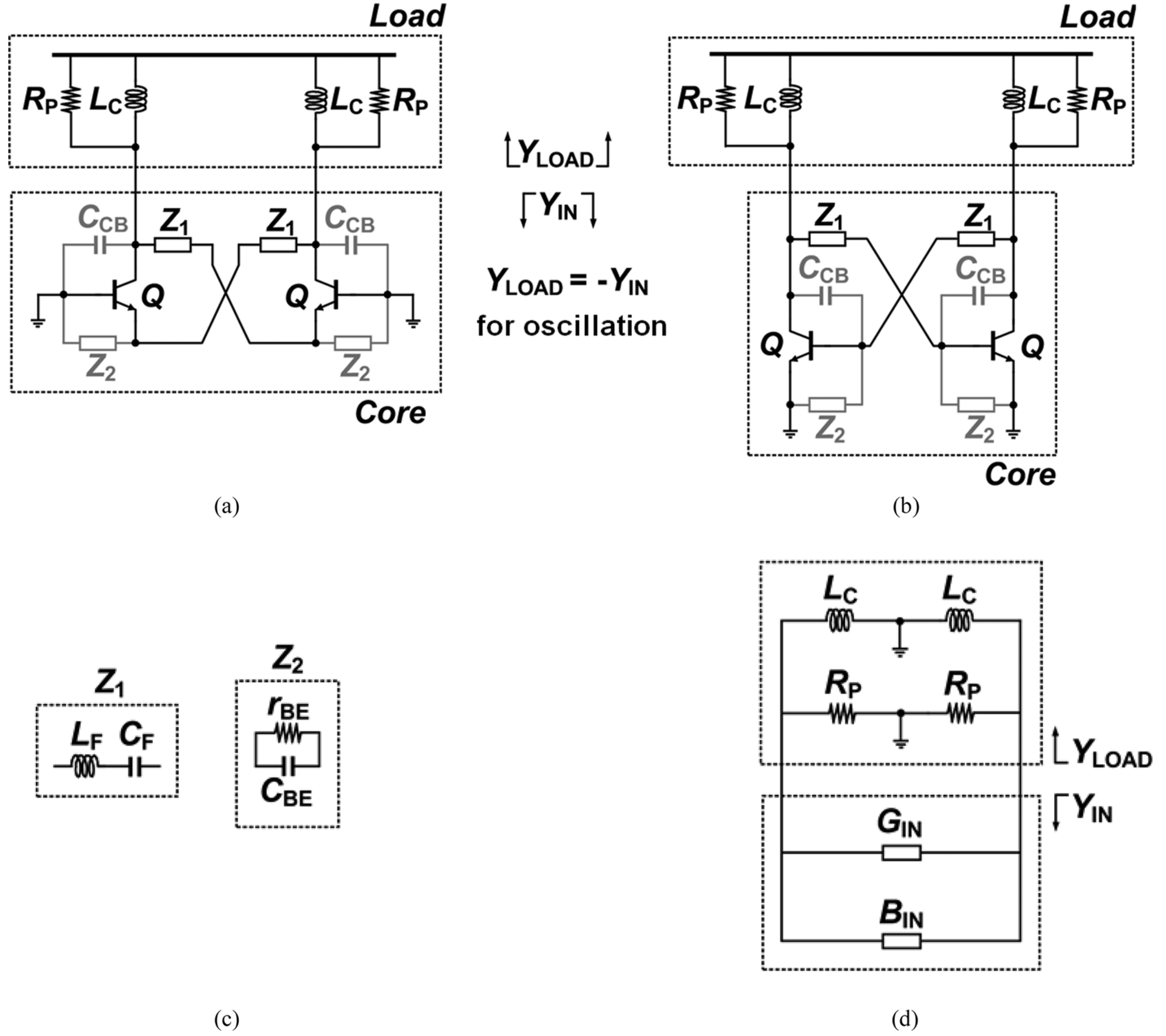

Fig. 4. Schematics used for the one-port analysis of cross-coupled oscillators. (a) CB configuration.(b) CE configuration.. (c) The components inside Z_1 and Z_2. (d) The equivalent circuit of (a) and (b) with the core represented by conductance and susceptance.

for cross-coupling can be exploited especially for high-speed transistors.

B. CB Versus CE for Cross-Coupling: Quantitative Comparison

For a quantitative comparison between CB and CE configurations for cross-coupling in oscillators in terms of the oscillation frequency, a one-port analysis for both configurations has been carried out in this work based on an analytic approach. Fig. 4(a) and (b) show the simplified schematics of the oscillator core for both CB and CE configurations. The circuit elements for the feedback impedance Z_1 and the intrinsic base-to-emitter impedance Z_2 are explicitly shown in Fig. 4(c). Fig. 4(d) provides an equivalent circuit applied for both configurations representing the core in terms of the conductance G_{IN} and the susceptance B_{IN}. The feedback impedance Z_1 comprises L_F and C_F, which are heavily weighted for this analysis while most other analyses mainly focus on the *LC* tank. The effect of these feedback components on the oscillation frequency is expected to be significant in high-frequency bands such as the THz band. C_F is needed for the bias purpose as well, particularly for the bipolar-based oscillation core for both CB and CE cases. To place an emphasis primarily on the oscillation core, the model was kept as simple as possible. For this purpose, the output buffer, contact resistances from the transistors, and the parasitic resistance of the feedback impedance are neglected in this model. Also, for the CB configuration, dc feedlines between the emitter and the ground are ignored to focus on the RF property of the oscillators. The load of each topology is assumed to be composed of inductance L_C and its parasitic resistance R_P.

First, the analysis is made for the CB cross-coupled oscillator. The input admittance Y_{IN} of the core is given as follows:

$$\begin{aligned} Y_{\mathrm{IN}} &= G_{\mathrm{IN}} + jB_{\mathrm{IN}} \\ &= \frac{1}{2}\left(\frac{1}{Z_1} + sC_{\mathrm{CB}} - \frac{\frac{1}{Z_1} - g_m}{Z_1\left(\frac{1}{Z_1} + \frac{1}{Z_2} + g_m\right)}\right) \end{aligned} \quad (1)$$

where $Z_1 = j\omega L_F + 1/j\omega C_F$, $Z_2 = 1/(j\omega C_{\mathrm{BE}} + 1/r_{\mathrm{BE}})$. When the parameters for Z_1 and Z_2 are substituted and the following approximations are made, $g_m \gg 1/r_{\mathrm{BE}}$, $g_m \gg |1/j\,(\omega L_F - 1/\omega C_F)|$, $|j\omega C_{\mathrm{BE}}| \gg |1/j\,(\omega L_F - 1/\omega C_F)|$,

$L_F C_{\mathrm{CB}} g_m^2 / C_{\mathrm{BE}}^2 \gg 1$, $\omega^2 L_F C_F (C_{\mathrm{BE}}^2(\omega^2 - 1/L_F C_F)/g_m^2 + 1) \gg 1$, then the real and the imaginary parts are obtained as follows:

$$G_{\mathrm{IN}} = Re(Y_{\mathrm{IN}}) = -\frac{\omega^2 C_F C_{\mathrm{BE}} g_m}{2(\omega^2 C_{\mathrm{BE}}^2 + g_m^2)(\omega^2 L_F C_F - 1)} \quad (2)$$

$$B_{\mathrm{IN}} = Im(Y_{\mathrm{IN}}) = \frac{L_F C_F C_{\mathrm{CB}} \omega^2 (C_{\mathrm{BE}}^2 \omega^2 + g_m^2) - (2C_F + C_{\mathrm{CB}}) g_m^2}{2 L_F C_F \omega (C_{\mathrm{BE}}^2 \omega^2 + g_m^2)}. \quad (3)$$

From (2), it is apparent that G_{IN} will show a negative value *above* a certain resonance frequency determined by L_F and C_F. Hence, it is expected that there exists a *lower* limit for the oscillation frequency. On the other hand, the load admittance Y_{LOAD} is given as

$$Y_{\mathrm{LOAD}} = G_{\mathrm{LOAD}} + jB_{\mathrm{LOAD}} = \frac{1}{2R_p} - j\left(\frac{1}{2\omega L_C}\right). \quad (4)$$

For the oscillation to occur, the condition $Y_{\mathrm{IN}} + Y_{\mathrm{LOAD}} = 0$ must be satisfied, for which both real and imaginary parts must meet the condition independently. When the imaginary part is considered, the oscillation frequency ω_{OSC} can be obtained by finding ω that meets the condition $B_{\mathrm{IN}} = -B_{\mathrm{LOAD}}$ using (3) and (4). With additional approximation, $L_C C_{\mathrm{CB}} g_m^2 / C_{\mathrm{BE}}^2 \gg 1$, the formula of ω_{OSC} is given as (5), shown at the bottom of the page. It looks a bit lengthy, but its further reduction will be possible only with approximations that can hardly be generally assumed with typical device parameters employed in this work, unlike other approximations made so far. When the real part is considered, the startup condition for the CB configuration can be found based on (2) and (4) as

$$|G_{\mathrm{IN}}| = \left| -\frac{\omega^2 C_F C_{\mathrm{BE}} g_m}{2(\omega^2 C_{\mathrm{BE}}^2 + g_m^2)(\omega^2 L_F C_F - 1)} \right| \geq \left| \frac{1}{2R_p} \right|. \quad (6)$$

Second, an analysis is made for the CE cross-coupled oscillator in a similar way as the CB case. Y_{IN} of the core is given as

$$Y_{\mathrm{IN}} = \frac{1}{2}\left(\frac{1}{Z_1} + sC_{\mathrm{CB}} + \frac{(sC_{\mathrm{CB}} - \frac{1}{Z_1})(\frac{1}{Z_1} - sC_{\mathrm{CB}} + g_m)}{\frac{1}{Z_1} + \frac{1}{Z_2} + sC_{\mathrm{CB}}}\right). \quad (7)$$

With the actual parameters substituted for Z_1 and Z_2 and the following approximations, $|1/j(\omega L_F - 1/\omega C_F)| \gg |j\omega C_{\mathrm{CB}}|$, $|j(\omega C_{\mathrm{BE}} - 1/(\omega L_F - 1/\omega C_F))| \gg 1/r_{\mathrm{BE}}$, $C_{\mathrm{BE}} \gg C_{\mathrm{CB}}$, G_{IN}, and B_{IN} are obtained as follows:

$$G_{\mathrm{IN}} = \mathrm{Re}(Y_{\mathrm{IN}}) = -\frac{C_F g_m}{2(C_F - C_{\mathrm{BE}}(\omega^2 L_F C_F - 1))} \quad (8)$$

$$B_{\mathrm{IN}} = \mathrm{Im}(Y_{\mathrm{IN}}) = \frac{C_F C_{\mathrm{BE}} \omega}{2(C_F - C_{\mathrm{BE}}(\omega^2 L_F C_F - 1))}. \quad (9)$$

From (8), a negative conductance will be observed *below* a certain resonance frequency determined by L_F, C_F, and C_{BE}. Hence, it is expected that there exists an *upper* limit in the oscillation frequency. Similar to the CB case, the oscillation frequency ω_{OSC} can be obtained from (9) and (4) using the condition $B_{\mathrm{IN}} = -B_{\mathrm{LOAD}}$

$$\omega_{\mathrm{OSC}} = \sqrt{\frac{1}{(L_F + L_C)}\left(\frac{1}{C_F} + \frac{1}{C_{\mathrm{BE}}}\right)}. \quad (10)$$

The startup condition for the CE configuration can be found from (8) and (4) as

$$|G_{\mathrm{IN}}| = \left| -\frac{C_F g_m}{2(C_F - C_{\mathrm{BE}}(\omega^2 L_F C_F - 1))} \right| \geq \left| \frac{1}{2R_P} \right|. \quad (11)$$

C. CB Versus CE for Cross-Coupling: Verification With Simulation

As seen in (2) and (6), G_{IN} is a function of frequency as well as various circuit and device parameters. In order to examine the trend of G_{IN} over frequency, its value was calculated from (2) and (6) with actual parameter values. The results are plotted in Fig. 5 for both CB and CE cases. The values inserted for the device parameters, g_m, C_{CB}, and C_{BE}, are 0.442 S, 5.4 fF, and 113.2 fF, respectively. These values were extracted based on [26] and [27] for a device with an emitter length of 5 μm, which was actually used for the fabricated circuit. Also, the values of 50 pH, 60 fF, and 50 pH are used for L_F, C_F, and L_C, respectively, which are roughly the same values as used for the actual oscillator design.

As can be seen from the inset of Fig. 5(a), G_{IN} for the CB case show a resonance peak near 100 GHz, above which it exhibits negative values. A similar peak is shown for G_{IN} with the CE case [inset of Fig. 5(b)], and the negative values are now shown below the resonance. This is consistent with what was expected from the analysis as indicated by (2) and (8). For a better observation of the actual value, the negative regions of G_{IN} are zoomed and plotted in Fig. 5 for both cases. They consistently show negative values for a wide range of frequency.

To verify the accuracy of the analyses performed in this work, results obtained from circuit simulation are added and compared to the calculated curves in Fig. 5. The simulation was made for the circuits shown in Fig. 4 with the transistor model provided by the design kit and ideal passive components. It is clear from the observation that the resonance frequency obtained from the calculation well matches that from the simulation for both CB and CE cases. In addition, reasonably good

$$\omega_{\mathrm{OSC}} = \sqrt{\frac{g_m\left(\sqrt{L_F L_C C_F C_{\mathrm{CB}}(L_F C_F (L_C C_{\mathrm{CB}} g_m^2 + 4C_{\mathrm{BE}}^2) + 4 L_C C_{\mathrm{BE}}^2 (2C_F + C_{\mathrm{CB}}))} - L_F L_C C_F C_{\mathrm{CB}} g_m\right)}{2 L_F L_C C_F C_{\mathrm{CB}} C_{\mathrm{BE}}^2}} \quad (5)$$

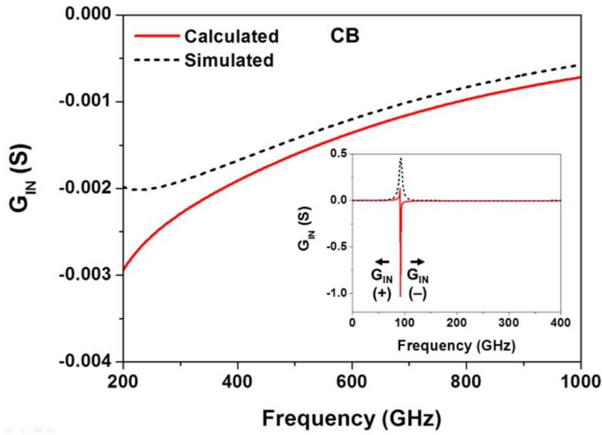

(a)

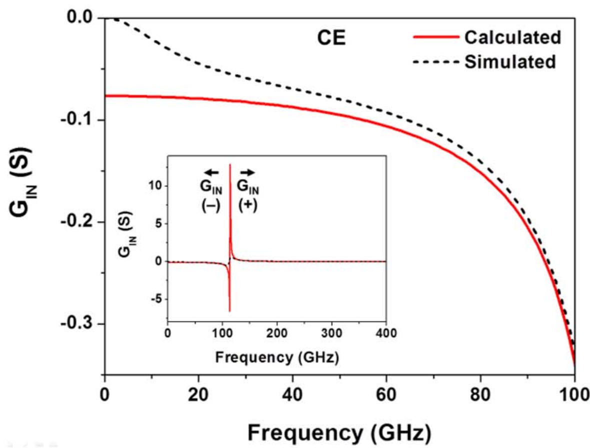

(b)

Fig. 5. $G_{\rm IN}$ of the cross-coupled core. (a) CB configuration. (b) CE configuration. Calculation is from analytic solutions (2) and (8). Simulation is based on transistor model from design kit.

agreements are shown for the values of $G_{\rm IN}$ for both cases, validating the accuracy of the analyses made in this work.

The oscillation frequency was also calculated based on (5) and (10) for both CB and CE cases, the results being displayed in Fig. 6. They are plotted as a function of three circuit parameters, L_F, C_F, and L_C, to observe the effect of each parameter on the oscillation frequency. It is clearly seen from the plots that the oscillator based on the CB configuration shows much higher oscillation frequency than the one based on the CE configuration. This is the major result obtained from the analyses made in this study. Furthermore, it is observed that the curves from the simulation closely match the calculation, validating the results obtained by the analysis made in this work. For the CB configuration, the oscillation frequency tends to be more affected by L_F and L_C, while the dependence on C_F appears to be stronger for the CE case. Hence, the design of CB-based oscillator may benefit from its insensitivity to C_F variation, and the value of C_F can be optimized solely for the output power independent of its effect on the oscillation frequency.

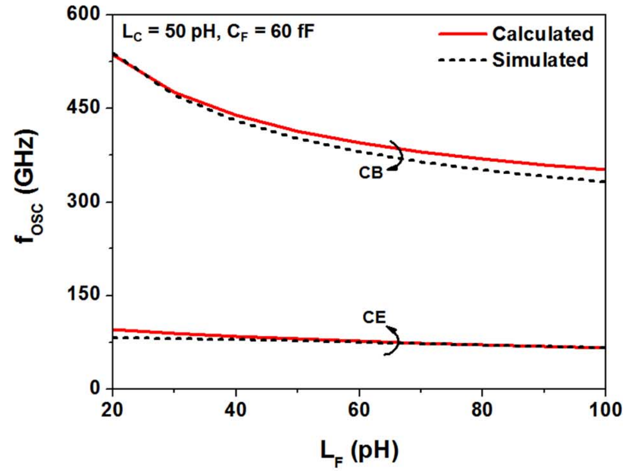

(a)

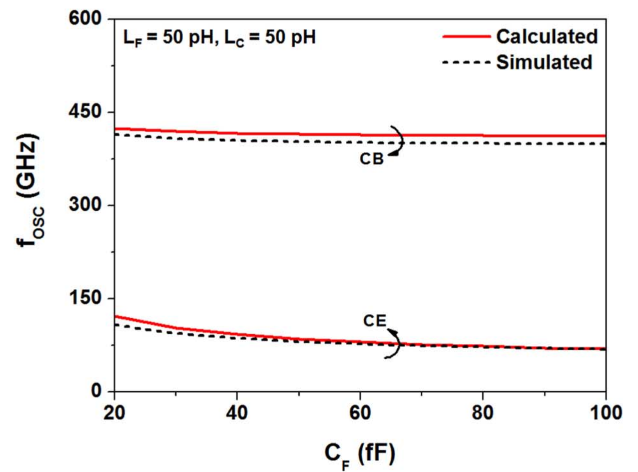

(b)

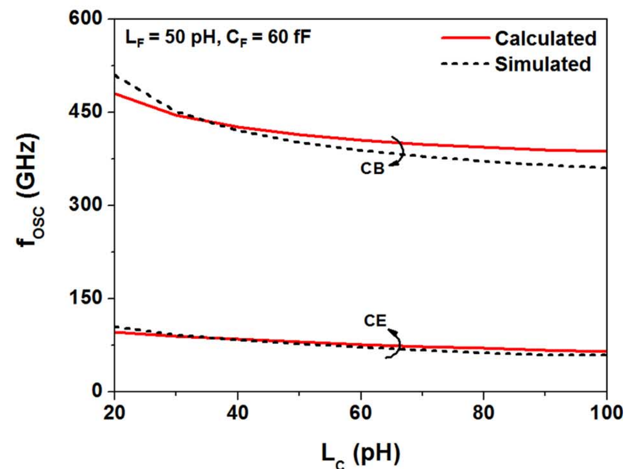

(c)

Fig. 6. Oscillation frequency of the CB and CE cross-coupled oscillator as a function of (a) L_C, (b) C_F, and (c) L_C. Calculation is from analytic solutions (5) and (10). Simulation is based on the transistor model from the design kit.

As an effort to better visualize the effect of L_F, C_F, and L_C on the oscillation frequency, contour plots of the oscillation frequency for both CB and CE cases were created and presented in Fig. 7. They show contours of constant oscillation frequency in the $L_F - C_F$ space for three different values of L_C: 20, 50, and 100 pH. The plots reveal that, by a proper combination of

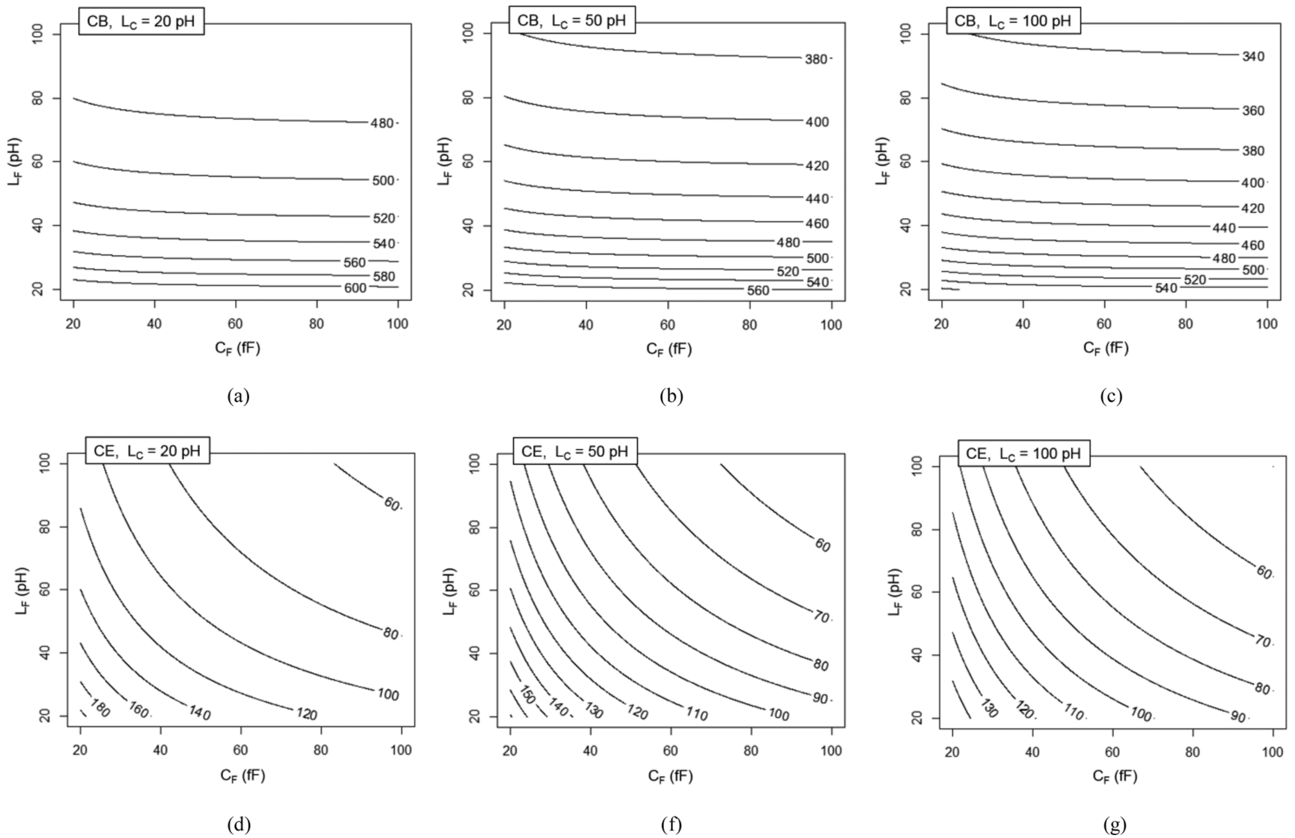

(a) (b) (c)

(d) (f) (g)

Fig. 7. Contour plots of oscillation frequency based on analytic solutions (5) and (10), drawn for (a)–(c) CB and (d)–(g) CE configurations with L_F and C_F variation. L_C is 20 pH for (a) and (d), 50 pH for (b) and (f), and 100 pH for (c) and (g). The frequencies for contours are shown in gigahertz.

L_F and C_F as well as with L_C, a wide range of oscillation frequency can be selected for design with the given topology for both CB and CE, although the range is substantially higher for the CB case. It is noted that the effect of the output buffer is not reflected on the plots. It is also noted that the results presented in Figs. 6 and 7 are based on the device with emitter length 5 μm, and the oscillation frequency level may be shifted up or down if different device sizes are applied.

D. Proposed Oscillators

Based on the analysis performed in this work, two CB cross-coupled oscillators were designed. The schematic of the proposed circuits, denoted as OSC1 and OSC2, are shown in Fig. 8. OSC1 and OSC2 are identical except for the fact that OSC2 includes varactors for frequency tuning. Hence, OSC1 is a fixed-frequency oscillator while OSC2 is a VCO. In the circuits, all the inductive elements were implemented with microstrip lines, which were used for the interconnection and resonant tank. $L_{1,2}$ are dc feedlines between the emitter of the core transistors $Q_{1,2}$ and the ground to allow dc current paths to the ground. $L_{F1,2}$ and $C_{F1,2}$ are components for the cross-coupled feedback. $C_{F1,2}$ also serve to isolate the collector of $Q_2(Q_1)$ and the emitter of $Q_1(Q_2)$ dc-wise for independent bias. $L_{3,4}$ are the loads of the oscillator, and they provide the signal paths to the stacked buffer, which is designed in the CB configuration. The buffer is composed of $Q_{3,4}$ and their own loads, $L_{5,6}$ and $L_{7,8}$, leading to the output nodes through blocking capacitors, $C_{DB1,2}$. This buffer is expected to additionally affect the oscillation frequency, which was not included in the analysis described earlier for simplicity. For OSC2, varactors are added to the emitter nodes of the oscillator core through $L_{V1,2}$, in order to provide voltage tuning and thus oscillation frequency tuning. Since varactors are not offered by the process technology used in this work, the base-collector junction of a bipolar transistor with the emitter shorted to the base was used as a varactor. The tuning voltage applied across the base and collector modulates the depletion width of the collector-base junction, leading to junction capacitance variation, a property of a varactor. Table I summarizes the values of the passive components that were used.

The transistor size was chosen considering two aspects: it should guarantee stable oscillation over 300 GHz, while it provides sufficient output power. Fig. 9 shows the simulated oscillation frequency and output power as a function of the emitter length, for OSC1 as an example. Simulation was carried out with a circuit simulator in the transient mode, where the changes in oscillation frequency and output power were observed. The device sizes of all four transistors $(Q_1–Q_4)$ were changed simultaneously. Overall, the output power grows with increasing emitter length, while it exhibits a sign of saturation for longer emitter lengths, degrading the dc-to-RF efficiency. On the other hand, the oscillation frequency rather monotonically drops as the device size is increased. Based on this result, the size of the transistors $Q_1–Q_4$ was chosen as 5 μm. It is noted that the oscillation frequency shown in Fig. 9 is substantially lower than what was shown in Fig. 7. Such discrepancy can be ascribed to

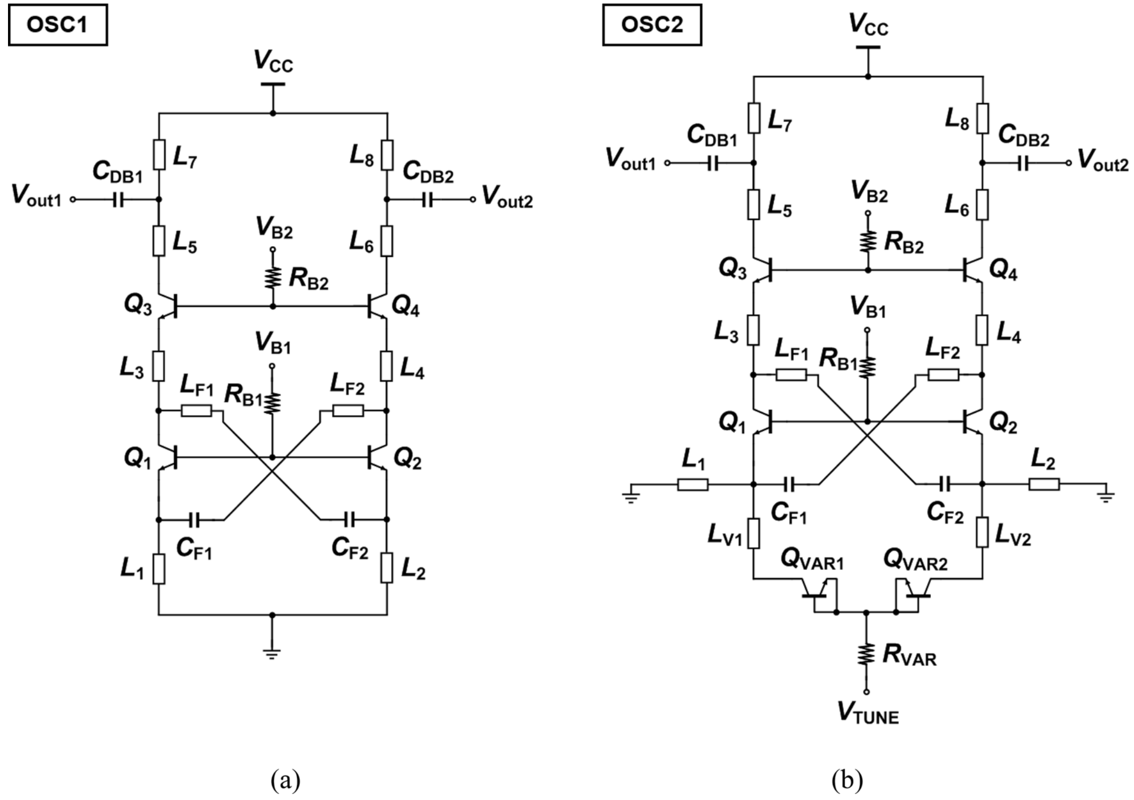

Fig. 8. Schematics of the proposed oscillators. (a) OSC1: a fixed-frequency oscillator. (b) OSC2: a voltage-controlled oscillator.

TABLE I
PASSIVE CIRCUIT PARAMETERS

	OSC1	OSC2		OSC1	OSC2
$L_{F1,2}$ (µm)	100	70	$L_{5,6}$ (µm)	35	35
$C_{F1,2}$ (fF)	60	60	$L_{7,8}$ (µm)	70	70
$L_{1,2}$ (µm)	60	45	$C_{DB1,2}$ (fF)	300	300
$L_{3,4}$ (µm)	70	80	$L_{V1,2}$ (µm)	-	40

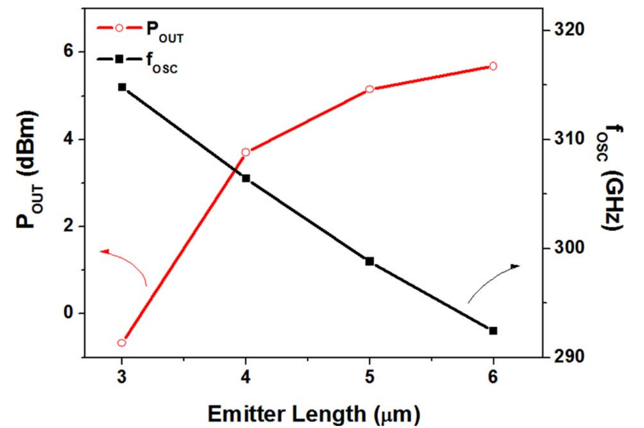

Fig. 9. Simulated oscillation frequency and output power as a function of device emitter length.

the buffer, which was not included for Fig. 7, because the parasitics of the buffer, especially C_{BE} of Q_3 and Q_4, are expected to influence the overall reactance seen by the oscillator core, leading to the oscillation frequency shift. Additionally, the parasitic base inductance, which was not considered for Fig. 7, also contributes to the difference. As will be seen in the next section, the simulation results provided in Fig. 9 show a good agreement with the measurement.

III. MEASUREMENT RESULTS

The two oscillators were fabricated in Teledyne 250-nm InP HBT technology, the details of which are provided in [26]. f_T and $f_{\max}$ are 392 and 859 GHz, respectively, from the device model. The die photographs of OSC1 and OSC2 are shown in Fig. 10(a) and (b), respectively. The chip size for each oscillator is 526×462 μm^2 and 518×431 μm^2, including dc and RF pads. It is noted that both circuits are designed to have differential outputs, but the measurement was carried out in a single-ended configuration with one of the output nodes terminated with 50Ω.

Fig. 11 shows the measurement setups employed in this work for the electrical characterization of the circuits. Fig. 11(a) is the setup for the measurement of the output spectrum and the phase noise, which were measured by an Agilent 4407B spectrum analyzer through a Virginia Diodes H-band (220–325 GHz) down conversion subharmonic mixer. The LO of the subharmonic mixer was driven by a Quinstar D-band (110–170 GHz) tripler that was powered by an Agilent E8257D signal generator. With the second-order subharmonic mixer used in this work, two oscillation frequencies may correspond to a single measured value

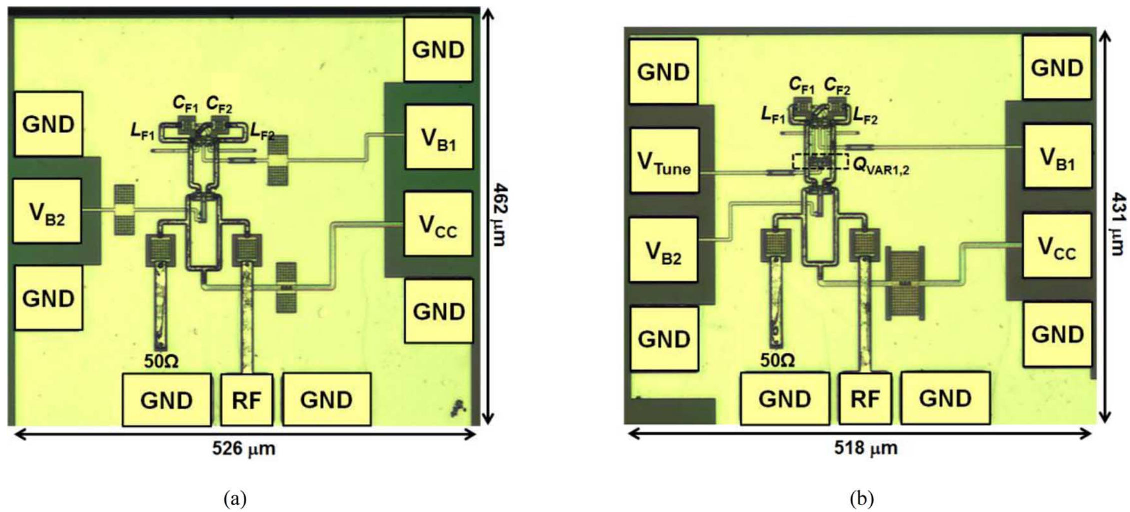

Fig. 10. Die phototograph of the fabricated circuits. (a) OSC1. (b) OSC2.

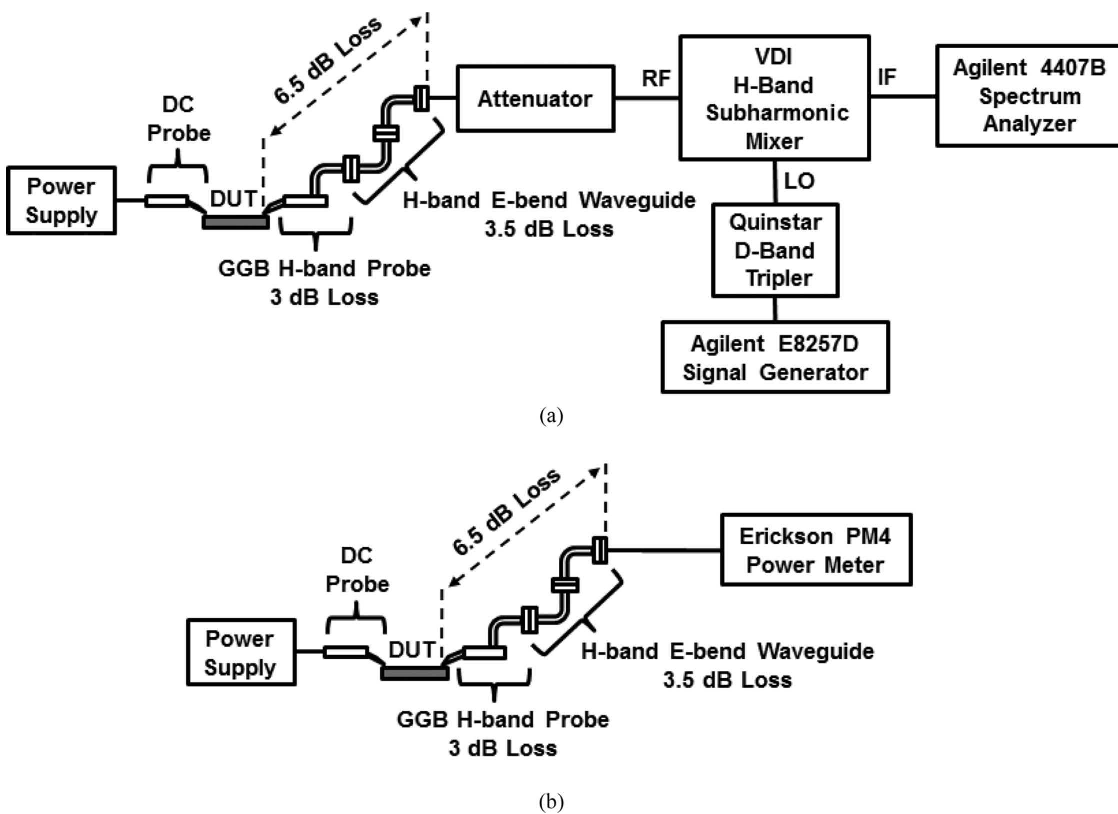

Fig. 11. Measurement setup for electrical characterization. (a) For output spectrum and phase noise. (b) For output power.

of $f_{\rm IF}$: $f_{\rm RF} = 2f_{\rm LO}+f_{\rm IF}$ and $f_{\rm RF} = 2f_{\rm LO}-f_{\rm IF}$. By observing the change in $f_{\rm IF}$ with $f_{\rm LO}$ variation, the correct $f_{\rm RF}$ value can be found, which was $2f_{\rm LO}-f_{\rm IF}$ in this paper. An attenuator was inserted in front of the down conversion mixer to maintain the RF input of the mixer below 10 μW, which was the maximum allowed input power of the mixer to avoid damage. Two E-bend waveguides were inserted between the attenuator and the GGB Industries H-band probe used for RF probing, which was necessary for vertical level shift of the waveguide path in the measurement setting employed. The total loss from the probe tip to the end of the E-bend waveguide chain was estimated to be 6.5 dB, which is the sum of the probe loss of 3 dB and the loss through the two waveguide bends of 3.5 dB. The RF probe loss is provided by the manufacturer, while the waveguides loss was determined by measurement. Fig. 11(b) is the setup for the measurement of the oscillator output power, which was directly measured by the Erickson PM4 power meter. Again, two E-bend waveguides were inserted between the H-band probe and the power meter for the same reason as described above.

Fig. 12 shows the measured output spectrum of the oscillators. For OSC1 and OSC2, $2f_{\rm LO}$ was set to 300 and 290 GHz, respectively. With these values for $2f_{\rm LO}$, the measured center

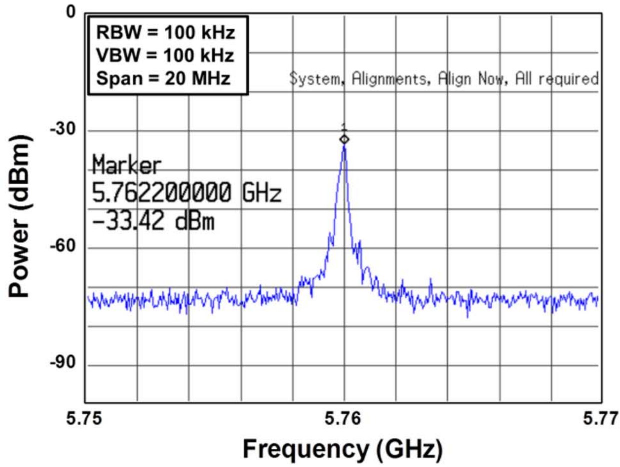

(a)

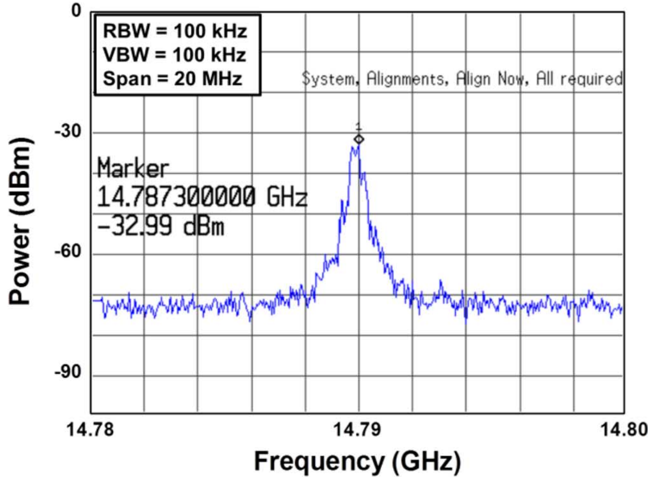

(b)

Fig. 12. Measured output spectrum. (a) OSC1. (b) OSC2.

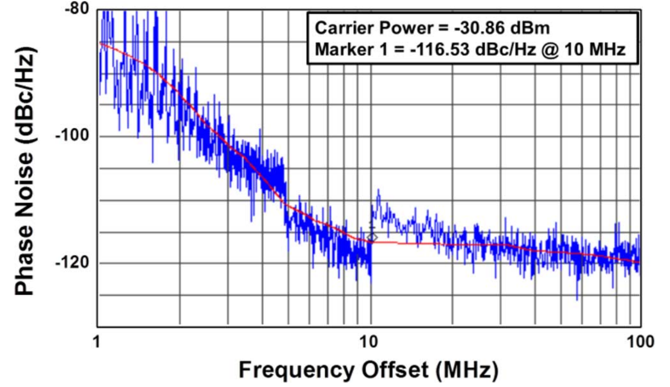

Fig. 13. Measured phase noise of OSC1.

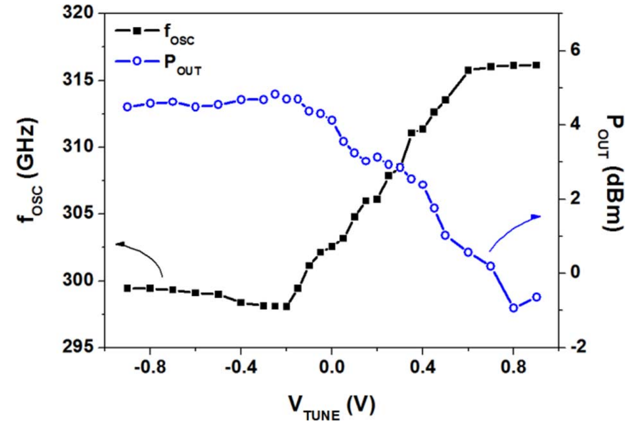

Fig. 14. Measured oscillation frequency and output power of OSC2 shown as a function of tuning voltage.

frequencies of 5.8 and 14.8 GHz indicated in the plots correspond to the oscillation frequencies of 305.8 and 304.8 GHz for OSC1 and OSC2 (with $V_{\rm TUNE} = 0.1$ V), respectively.

Phase noise measurement at this high-frequency band is not trivial, and much care needs to be taken. In this work, the phase noise of OSC1 was measured with the down-converted signal with the setup shown in Fig. 11(a). With such a setup, the phase noise of the LO signal applied to the mixer may contribute to the measured phase noise. However, a simple calculation shows that the phase noise of the LO is far lower than the measured phase noise with the typical phase noise level of the signal generator and the multiplication factor, and thus its effect can be ignored. The measured phase noise of the oscillator is shown in Fig. 13, which exhibits -116.5 dBc/Hz at 10-MHz offset. It is noted that the phase noise value varied over different measurement attempts, and it roughly fell in the range of -112.3 to -116.5 dBc/Hz at 10-MHz offset. For the case of OSC2, which is a VCO, a reliable phase noise plot was not available because the signal was less stable than that of OSC1 as it is sensitive to $V_{\rm TUNE}$ fluctuation. However, a rough estimation of its phase noise can be made by comparing its spectrum [Fig. 12(b)] with that of the oscillator [Fig. 12(a)], which reveals that the phase noise is slightly worse for OSC2, while the difference appears not excessive.

The output power of the circuits was directly measured by a PM4 power meter with the setup shown in Fig. 11(b). The direct measurement avoids the uncertainties related to the losses in the attenuator, mixer, and IF port cable that would affect any power measurement made using the setup in Fig. 11(a). The measured output power of OSC1 is 5.3 dBm. It is noted that power loss of 6.5 dB from the RF probe and waveguides, as mentioned earlier, is compensated for in the measured data. It is also noted that the measured output power is for the single-ended output, and no value conversion was made for the differential output case. For the case of OSC2, the measured output power varies from 4.8 to -0.9 dBm, depending on $V_{\rm TUNE}$, as indicated by Fig. 14. The dc power consumption of OSC1 and OSC2 is 87.4 and 88.1 mW, leading to a dc-to-RF efficiency of 3.9 and 3.4%, respectively. Fig. 14 also shows the tuning profile of OSC2 as a function of $V_{\rm TUNE}$. Its oscillation frequency was tuned from 298.1 to 316.1 GHz with $V_{\rm TUNE}$ swept from -0.2 V to 0.8 V, leading to a total tuning range of 18 GHz. To the authors' knowledge, OSC1and OSC2 presented in this paper show the highest output power and dc-to-RF efficiency for any transistor-based semiconductor oscillator operating above 200 GHz without power combining.

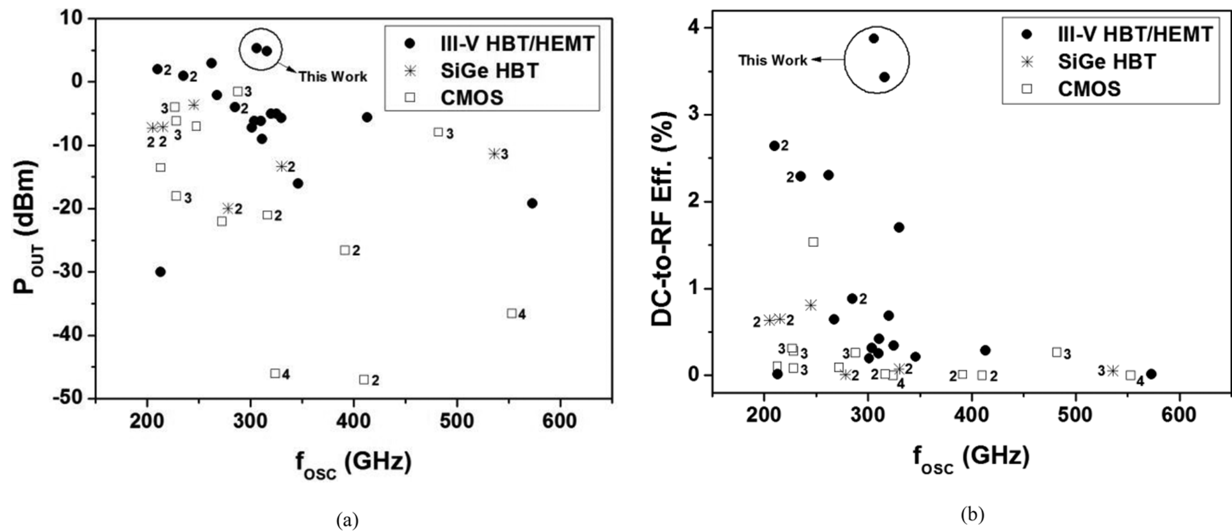

Fig. 15. Comparison of the oscillators developed in this paper with the literature. (a) Output power. (b) dc-to-RF efficiency of single sources (without power combining) above 200 GHz. The numbers next to symbols indicate the harmonic number.

TABLE II
SINGLE SOURCES OPERATING AT H-BAND AND HIGHER

Reference	Technology	Harmonic Number	Frequency (GHz)	Peak P_{OUT} (dBm)	P_{dc} (mW)	dc-to-RF Efficiency (%)	Phase Noise at10 MHz (dBc/Hz)
[28]	32 nm CMOS	1	272	-22	7	0.09	-
[29]	65 nm CMOS	3	288	-1.5	275	0.26	-87*
[14]	65 nm CMOS	3	482	-7.9	61	0.27	-76*
[21]	120 nm SiGe HBT	1	218-245	-3.6	54	0.81	-98
[21]	120 nm SiGe HBT	2	309-330	-13.3	63	0.07	-78
[19]	130 nm SiGe HBT	3	519-536	-11.3	156.3	0.05	-
[10]	250 nm InP HBT	1	573.1	-19.2	76-115	0.01	-
[11]	250 nm InP HBT	1	325	-5	92.4	0.34	-90.4
[12]	35 nm InP HEMT	1	330	-5.7	15.9	1.7	-
This work	250 nm InP HBT	1	305.8	5.3	87.4	3.88	-116.5
This work	250 nm InP HBT	1	298.1-316.1	4.8	88.1	3.43	-

* Phase noise at 1 MHz offset

Table II compares the performance of the developed oscillators in this paper with other recently reported state-of-the-art oscillators operating at H-band and higher. The results with multiplier chains and oscillators with output power combining are not included. As can be seen in the table, the oscillators developed in this paper exhibit the leading performance in terms of the output power and the dc-to-RF efficiency as well as the phase noise level. Such comparison is better illustrated in Fig. 15, which plots the output power and the dc-to-RF efficiency obtained in this paper together with the single sources (without power combining) reported above 200 GHz [12]–[14], [16], [17], [28]–[44].

IV. IMAGING EXPERIMENT

Terahertz imaging is one of the applications that would require high output power signal sources operating at the high-frequency band. In order to examine the practical applicability of the developed circuits, a transmission-mode THz imaging experiment has been carried out with OSC1. The imaging setup built for the study is depicted in Fig. 16, which employs the fabricated oscillator as a source and an Erickson PM4 power meter as a detector. The target object for imaging is attached to a moving stage which is controlled by a computer for a 2-D raster scan. One key feature of this setup is that images can be obtained through on-wafer probing with an external horn antenna. The integration of on-chip antennas and the packaging of the chips with wire-bonding may induce various uncertainties, which can be avoided with this setup. Moreover, the setup allows a quick evaluation of imaging compatibility of fabricated circuits while saving the chips for other repeated on-wafer electrical tests.

For imaging, the output signal from the oscillator was extracted via the RF probe and waveguides and then radiated through the horn antenna. The radiated signal was then transmitted through the scanned object and received by another horn antenna attached to the PM4 power meter. The distance between the two horn antennas was set to 4 cm, and the target object was placed at the midpoint. With this kind of short range imaging arrangement, the need for the optical focusing can be eliminated.

Fig. 17 shows the images acquired with this setup, for which the scan step was set to 300 μm. Two target objects based on a floppy disk and a knife were used for the imaging. The objects were enclosed inside a paper envelope before the images were taken. The obtained images reveal the well-known unique properties of the THz waves, namely the transmission through paper

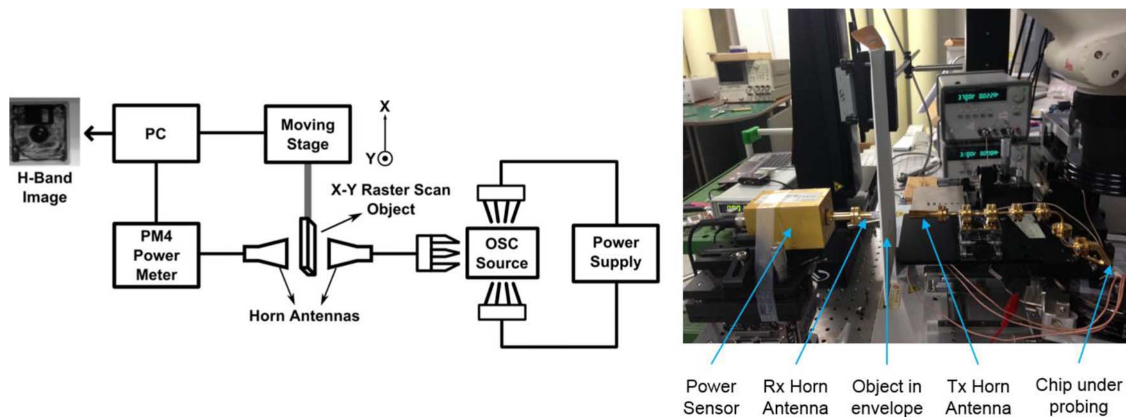

Fig. 16. Setup for the imaging experiment.

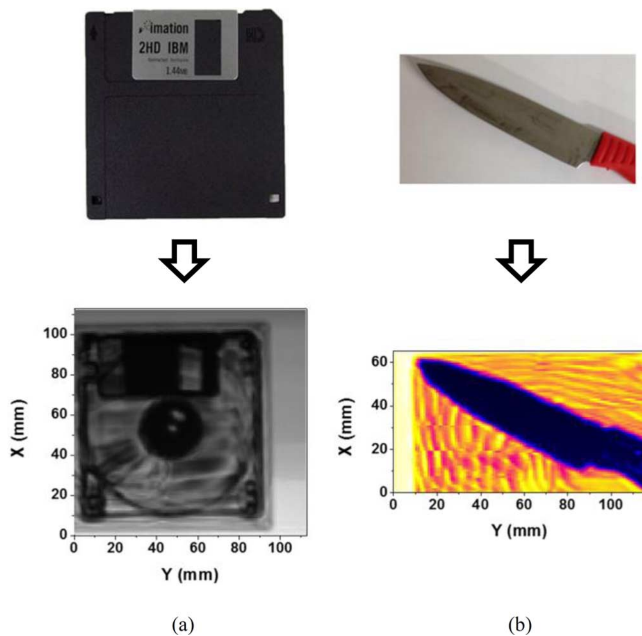

Fig. 17. Images obtained in this work. (a) Floppy disk. (b) Knife. All objects were placed in a paper envelope during imaging experiment.

and plastic and reflection by metal. As can be seen in the figure, the internal structure of the floppy disc is well visible, and the shape of the knife can be clearly seen although they were all enclosed inside a paper envelope. The results show that the fabricated oscillator can be well applied for THz imaging.

V. Conclusion

A fixed-frequency oscillator and a VCO operating near 300 GHz in a fundamental-mode have been developed based on an InP HBT technology. Both oscillators adopted a common-base cross-coupled topology for oscillation, which were shown to outperform the conventional common-emitter cross-coupled topology by analytical analysis as well as simulation in this study. Output power up to 5.3 dBm was obtained from the fabricated oscillators, which is the highest among the transistor-based oscillators operating beyond 200 GHz. Furthermore, application of the developed oscillator for THz imaging was successfully demonstrated. This work further expands the performance level of the solid-state THz signal sources and promises their various applications in the THz regime.

References

[1] P. H. Siegel, "Terahertz technology in biology and medicine," *IEEE Trans. Microw. Theory Techn.*, vol. 52, no. 10, pp. 2438–2447, Oct. 2004.

[2] J. Rieh *et al.*, "SiGe heterojunction bipolar transistors and circuits toward terahertz communication applications," *IEEE Trans. Microw. Theory Techn.*, vol. 52, no. 10, pp. 2390–2408, Oct. 2004.

[3] J. Nishizawa, P. Plotka, H. Makabe, and T. Kurabayashi, "GaAs TUNNETT diodes oscillating at 430-655 GHz in CW fundamental mode," *IEEE Microw. Compon. Lett.*, vol. 15, no. 9, pp. 597–599, Sep. 2005.

[4] H. Eisele, "480 GHz oscillator with an InP Gunn device," *Electron. Lett.*, vol. 46, pp. 422–423, 2010.

[5] M. Asada and S. Suzuki, "Resonant tunneling diodes for room-temperature terahertz oscillators," in *Proc. APMC Asia-Pacific Microwave Conf.*, 2013, pp. 345–347.

[6] J. O. Plouchart, "Applications of SOI technologies to communication," presented at the IEEE Compound Semicond. Integr. Circuit Symp., 2011.

[7] B. Heinemann *et al.*, "SiGe HBT technology with fT/fmax of 300GHz/500GHz and 2.0 ps CML gate delay," in *Proc. IEEE Int. Electron Devices Meeting*, 2010, pp. 30.5.1–30.5.4.

[8] M. Urteaga *et al.*, "InP HBTs for THz frequency integrated circuits," presented at the IEEE Int. Conf. Indium Phosphide Related Materials, 2011.

[9] R. Lai *et al.*, "Sub 50 nm InP HEMT device with fmax greater than 1 THz," in *Proc. IEEE Int. Electron Devices Meeting*, 2007, pp. 609–611.

[10] M. Seo *et al.*, "InP HBT IC technology for terahertz frequencies: Fundamental oscillators up to 0.57 THz," *IEEE J. Solid-State Circuits*, vol. 46, no. 10, pp. 2203–2214, Oct. 2011.

[11] J. Kim, H. Song, K. Ajito, M. Yaita, and N. Kukutsu, "A 325 GHz quadrature voltage controlled oscillator with superharmonic-coupling," *IEEE Microw. Compon. Lett.*, vol. 23, no. 8, pp. 430–432, Aug. 2013.

[12] V. Radisic *et al.*, "A 330-GHz MMIC oscillator module," in *IEEE MTT-S Int. Microw. Symp. Dig.*, 2008, pp. 395–398.

[13] H. Daquan *et al.*, "Terahertz CMOS frequency generator using linear superposition technique," *IEEE J. Solid-State Circuits*, vol. 43, no. 12, pp. 2730–2738, Dec. 2008.

[14] E. Seok *et al.*, "A 410GHz CMOS push-push oscillator with an on-chip patch antenna," in *IEEE ISSCC Dig. Tech. Papers*, 2008, pp. 472–629.

[15] B. Razavi, "A 300-GHz fundamental oscillator in 65-nm CMOS technology," *IEEE J. Solid-State Circuits*, vol. 46, no. 4, pp. 894–903, Apr. 2011.

[16] D. Shim, D. Koukis, D. J. Arenas, D. B. Tanner, and K. O. Kenneth, "553-GHz signal generation in CMOS using a quadruple-push oscillator," in *Proc. IEEE Symp. VLSI Circuits*, 2011, pp. 154–155.

[17] D. Shim *et al.*, "Components for generating and phase locking 390-GHz signal in 45-nm CMOS," in *Proc. IEEE Symp. VLSI Circuits*, 2012, pp. 10–11.

[18] O. Momeni and E. Afshari, "High power terahertz and millimeter-wave oscillator design: A systematic approach," *IEEE J. Solid-State Circuits*, vol. 46, no. 3, pp. 583–597, Mar. 2011.

[19] U. R. Pfeiffer *et al.*, "A 0.53THz reconfigurable source array with up to 1mW radiated power for terahertz imaging applications in 0.13mm SiGe BiCMOS," in *IEEE ISSCC Dig. Tech. Papers*, 2014, pp. 256–257.

[20] Y. Tousi and E. Afshari, "A scalable THz 2D phased array with +17 dBm of EIRP at 338 GHz in 65 nm bulk CMOS," in *IEEE ISSCC Dig. Tech. Papers*, 2014, pp. 258–259.

[21] S. P. Voinigescu *et al.*, "A study of SiGe HBT signal sources in the 220-330-GHz range," *IEEE J. Solid-State Circuits*, vol. 48, no. 9, pp. 2011–2021, Sep. 2013.

[22] E. Ojefors, J. Grzyb, Y. Zhao, B. Heinemann, B. Tillack, and U. R. Pfeiffer, "A 820 GHz SiGe chipset for terahertz active imaging applications," in *IEEE ISSCC Dig. Tech. Papers*, 2011, pp. 224–226.

[23] O. Momeni and E. Afshari, "A broadband mm-Wave and terahertz traveling-wave frequency multiplier on CMOS," *IEEE J. Solid-State Circuits*, vol. 46, no. 12, pp. 2966–2976, Dec. 2011.

[24] E. Ojefors, B. Heinemann, and U. R. Pfeiffer, "Active 220- and 325-GHz frequency multiplier chains in an SiGe HBT technology," *IEEE Trans. Microw. Theory Techn.*, vol. 59, no. 5, pp. 1311–1318, May 2011.

[25] F. Golcuk, O. D. Gurbuz, and G. M. Rebeiz, "A 0.39–0.44 THz 2×4 amplifier-quadrupler array with peak EIRP of 3-4 dBm," *IEEE Trans. Microw. Theory Techn.*, vol. 61, no. 12, pp. 4483–4491, Dec. 2013.

[26] M. Rodwell *et al.*, "Frequency Limits of InP-based Integrated Circuits," in *Proc. IEEE Int. Conf. Indium Phosphide Related Materials*, 2007, pp. 9–13.

[27] D. R. Pehlke and D. Pavlidis, "Evaluation of the factors determining HBT high-frequency performance by direct analysis of S-parameter data," *IEEE Trans. Microw. Theory Techn.*, vol. 40, no. 12, pp. 2367–2373, Dec. 1992.

[28] N. Landsberg and E. Socher, "240 GHz and 272 GHz fundamental VCOs using 32 nm CMOS technology," *IEEE Trans. Microw. Theory Techn.*, vol. 61, no. 12, pp. 4461–4471, Dec. 2013.

[29] J. Grzyb, Y. Zhao, and U. R. Pfeiffer, "A 288-GHz lens-integrated balanced triple-push source in a 65-nm CMOS technology," *IEEE J. Solid-State Circuits*, vol. 48, no. 7, pp. 1751–1761, Jul. 2013.

[30] S. Muralidharan and M. Hella, "A 213GHz-228GHz, −91 dB/Hz phase noise triple push oscillator in 65 nm CMOS," in *Proc. IEEE ISCAS Int. Symp. Circuits Syst.*, 2012, pp. 1062–1065.

[31] J. Sharma and H. Krishnaswamy, "216- and 316-GHz 45-nm SOI CMOS signal sources based on a maximum-gain ring oscillator topology," *IEEE Trans. Microw. Theory Techn.*, vol. 61, no. 1, pp. 492–504, Jan. 2013.

[32] B. Khamaisi and E. Socher, "A 209-233 GHz frequency source in 90 nm CMOS technology," *IEEE Microw. Compon. Lett.*, vol. 22, no. 5, pp. 260–262, May 2012.

[33] N. Landsberg and E. Socher, "A 234–248 GHz power efficient fundamental VCO using 32 nm CMOS SOI technology," in *IEEE MTT-S Int. Microw. Symp. Dig.*, 2013, pp. 1–3.

[34] B. Khamaisi, S. Jameson, and E. Socher, "A 210-227 GHz transmitter with integrated on-chip antenna in 90 nm CMOS technology," *IEEE Trans. Thz Sci. Technol.*, vol. 3, no. 2, pp. 141–150, Mar. 2013.

[35] Z. Wang, P. Chiang, P. Nazari, C. Wang, Z. Chen, and P. Heydari, "A 210 GHz fully integrated differential transceiver with fundamental-frequency VCO in 32 nm SOI CMOS," in *IEEE ISSCC Dig. Tech. Papers*, 2013, pp. 136–137.

[36] R. Wanner, R. Lachner, G. R. Olbrich, and P. Russer, "A SiGe monolithically integrated 278 GHz push-push oscillator," in *IEEE MTT-S Int. Microw. Symp. Dig.*, 2007, pp. 333–336.

[37] P. Chiang, O. Momeni, and P. Heydari, "A highly efficient 0.2 THz varactor-less VCO with −7 dBm output power in 130 nm SiGe," in *Proc. IEEE Compound Semicond. Integr. Circuit Symp.*, 2012, pp. 1–4.

[38] P. Chiang, O. Momeni, and P. Heydari, "A 200-GHz inductively tuned VCO with −7dBm output power in 130-nm SiGe BiCMOS," *IEEE Trans. Microw. Theory Techn.*, vol. 61, no. 10, pp. 3666–3673, Oct. 2013.

[39] M. Seo *et al.*, "> 300 GHz fixed-frequency and voltage-controlled fundamental oscillators in an InP DHBT process," in *IEEE MTT-S Int. Microw. Symp. Dig.*, 2010, pp. 272–275.

[40] V. Radisic *et al.*, "Demonstration of sub-millimeter wave fundamental oscillators using 35-nm InP HEMT technology," *IEEE Microw. Compon. Lett.*, vol. 17, no. 3, pp. 223–225, Mar. 2007.

[41] V. Radisic *et al.*, "Demonstration of a 311-GHz fundamental oscillator using InP HBT technology," *IEEE Trans. Microw. Theory Techn.*, vol. 55, no. 11, pp. 2329–2335, Nov. 2007.

[42] S. E. Rosenbaum *et al.*, "155- and 213-GHz AlInas/GaInAs/InP HEMT MMIC oscillators," *IEEE Trans. Microw. Theory Techn.*, vol. 43, no. 4, pp. 927–932, Apr. 1995.

[43] J. Kim, H. Song, K. Ajito, M. Yaita, and N. Kukutsu, "InP HBT voltage controlled oscillator for 300-GHz-band wireless communications," in *Proc. ISOCC Int. SoC Design Conf.*, 2012, pp. 262–265.

[44] Y. Baeyens *et al.*, "Highly efficient harmonically tuned inp D-HBT push-push oscillators operating up to 287 GHz," in *IEEE MTT-S Int. Microw. Symp. Dig.*, 2007, pp. 341–344.

Jongwon Yun received the B.S. degree from the School of Electrical Engineering, Korea University, Seoul, Korea, in 2007, where he is currently working toward the Ph.D. degree, under the supervision of Prof. Jae-Sung Rieh.

His primary research interests concern mm-wave and terahertz integrated circuits and systems for imaging and broadband communication applications.

Daekeun Yoon received the B.S. degree from the School of Electrical Engineering, Korea University, Seoul, Korea, in 2006, where he is currently working toward the Ph.D. degree, under the supervision of Prof. Jae-Sung Rieh.

His key research interests are mm-wave and terahertz integrated circuits for imaging and transceiver systems.

Hyunchul Kim received the B.S. and M.S. degree from the School of Electrical Engineering, Korea University, Seoul, Korea, in 2009 and 2013, respectively. He is currently working toward the Ph.D. degree in electrical engineering at the Virginia Polytech Institute and and State University, Blacksburg, VA, USA.

His major research interests are mm-wave integrated circuits and systems.

Jae-Sung Rieh (S'89–M'91–SM'05) received the B.S. and M.S. degrees in electronics engineering from Seoul National University, Seoul, Korea, in 1991 and 1995, respectively, and the Ph.D. degree in electrical engineering from the University of Michigan, Ann Arbor, MI, USA, in 1999.

In 1999, he joined the IBM Semiconductor R&D Center, where he was responsible for research and development activities for the high-frequency SiGe HBT technologies. Since 2004, he has been with the School of Electrical Engineering, Korea University, Seoul, Korea, where he is currently a Professor. In 2012, he was with Submillimeter Wave Advanced Technology team (SWAT), Jet Propulsion Laboratory, Pasadena, CA, USA, during his sabbatical leave. His major research interest lies in mm-wave and terahertz devices and circuits.

Dr. Rieh was a recipient of the 2004 IBM Faculty Award and a corecipient of the 2002 and 2006 IEEE Electron Device Society George E. Smith Awards and the 2013 IEEE Microwave and Wireless Component Letters Tatsuo Itoh Best Paper Award. He has served as an Associate Editor of the IEEE MICROWAVE AND WIRELESS COMPONENTS LETTERS (2006–2009) and the IEEE TRANSACTIONS ON MICROWAVE THEORY AND TECHNIQUES (2010–2013).